AFRL-RX-WP-JA-2015-0123

MICROSTRUCTURE AND ELEVATED TEMPERATURE PROPERTIES OF A REFRACTORY TaNbHfZrTi ALLOY (POSTPRINT)

D.B. Miracle and C.F. Woodward
AFRL/RXCM

O.N. Senkov, J.M. Scott, S.V. Senkova and F. Meisenkothen
UES, Inc.

APRIL 2014
Interim Report

AIR FORCE RESEARCH LABORATORY
MATERIALS AND MANUFACTURING DIRECTORATE
WRIGHT-PATTERSON AIR FORCE BASE OH 45433-7750
AIR FORCE MATERIEL COMMAND
UNITED STATES AIR FORCE

NOTICE AND SIGNATURE PAGE

//Signature//   //Signature//
_____   _____
MICHEAL E. BURBA, Project Engineer   DANIEL J. EVANS, Chief
Metals Branch   Metals Branch
Structural Materials Division   Structural Materials Division

//Signature//
_____
ROBERT T. MARSHALL, Deputy Chief
Structural Materials Division
Materials And Manufacturing Directorate

REPORT DOCUMENTATION PAGE

Form Approved
OMB No. 0704-0188

The public reporting burden for this collection of information is estimated to average 1 hour per response, including the time for reviewing instructions, searching existing data sources, gathering and maintaining the data needed, and completing and reviewing the collection of information. Send comments regarding this burden estimate or any other aspect of this collection of information, including suggestions for reducing this burden, to Department of Defense, Washington Headquarters Services, Directorate for Information Operations and Reports (0704-0188), 1215 Jefferson Davis Highway, Suite 1204, Arlington, VA 22202-4302. Respondents should be aware that notwithstanding any other provision of law, no person shall be subject to any penalty for failing to comply with a collection of information if it does not display a currently valid OMB control number. **PLEASE DO NOT RETURN YOUR FORM TO THE ABOVE ADDRESS**.

1. REPORT DATE *(DD-MM-YY)*	2. REPORT TYPE	3. DATES COVERED *(From - To)*
April 2014	Interim	19 March 2014 – 31 March 2014

4. TITLE AND SUBTITLE
MICROSTRUCTURE AND ELEVATED TEMPERATURE PROPERTIES OF A REFRACTORY TaNbHfZrTi ALLOY (POSTPRINT)

5a. CONTRACT NUMBER
In-house

5b. GRANT NUMBER

5c. PROGRAM ELEMENT NUMBER
62102F

6. AUTHOR(S)
D.B. Miracle and C.F. Woodward – AFRL/RXCM
O.N. Senkov, J.M. Scott, S.V. Senkova, and F.Meisenkothen – UES, Inc.

5d. PROJECT NUMBER
4349

5e. TASK NUMBER

5f. WORK UNIT NUMBER
X0W6

7. PERFORMING ORGANIZATION NAME(S) AND ADDRESS(ES)

AFRL/RXCM
2941 Hobson Way
Bldg 654, Rm 136
Wright-Patterson AFB, OH 45433

UES Inc.
4401 Dayton-Xenia Rd.
Dayton, OH 45432-1894

8. PERFORMING ORGANIZATION REPORT NUMBER

9. SPONSORING/MONITORING AGENCY NAME(S) AND ADDRESS(ES)

Air Force Research Laboratory
Materials and Manufacturing Directorate
Wright-Patterson Air Force Base, OH 45433-7750
Air Force Materiel Command
United States Air Force

10. SPONSORING/MONITORING AGENCY ACRONYM(S)
AFRL/RXCM

11. SPONSORING/MONITORING AGENCY REPORT NUMBER(S)
AFRL-RX-WP-JA-2015-0123

12. DISTRIBUTION/AVAILABILITY STATEMENT
Distribution Statement A. Approved for public release; distribution unlimited.

14. ABSTRACT
Compression properties of a refractory multicomponent alloy, $Ta_{20}Nb_{20}Hf_{20}Zr_{20}Ti_{20}$, were determined in the temperature range of 296–1473 K and strain rate range of 10^{-1}–10^{-5} s^{-1}. The properties were correlated with the microstructure developed during compression testing. The alloy was produced by vacuum arc melting, and it was hot isostatically pressed (HIPd) and homogenized at 1473 K for 24 h prior to testing. It had a single-phase body-centered cubic structure with the lattice parameter $a = 340.4$ pm. The grain size was in the range of 100–200 μm. During compression at a strain rate of $'\varepsilon = 10^{-3}$ s^{-1}, the alloy had the yield strength of 929 MPa at 296 K, 790 MPa at 673 K, 675 MPa at 873 K, 535 MPa at 1073 K, 295 MPa at 1273 K and 92 MPa at 1473 K. Continuous strain hardening and good ductility ($\varepsilon \geq 50\%$) were observed in the temperature range from 296 to 873 K. Deformation at $T = 1073$ K and $'\varepsilon \geq 10^{-3}$ s^{-1} was accompanied by intergranular cracking and cavitation, which was explained by insufficient dislocation and diffusion mobility to accommodate grain boundary sliding activated at this temperature. The intergranular cracking and cavitation disappeared with an increase in the deformation temperature to 1273 and 1473 K or a decrease in the strain rate to ~10^{-5} s^{-1}. At these high temperatures and/or low-strain rates the alloy deformed homogeneously and showed steady-state flow at a nearly constant flow stress. Partial dynamic recrystallization, leading to formation of fine equiaxed grains near grain boundaries, was observed in the specimens deformed at1073 and 1273 K and completed dynamic recrystallization was observed at 1473 K.

15. SUBJECT TERMS
high entropy alloys, alloy design, mechanical properties

16. SECURITY CLASSIFICATION OF:

a. REPORT	b. ABSTRACT	c. THIS PAGE
Unclassified	Unclassified	Unclassified

17. LIMITATION OF ABSTRACT:
SAR

18. NUMBER OF PAGES
16

19a. NAME OF RESPONSIBLE PERSON (Monitor)
Micheal E. Burba

19b. TELEPHONE NUMBER *(Include Area Code)*
(937) 255-9795

Standard Form 298 (Rev. 8-98)
Prescribed by ANSI Std. Z39-18

Microstructure and elevated temperature properties of a refractory TaNbHfZrTi alloy

**O. N. Senkov · J. M. Scott · S. V. Senkova ·
F. Meisenkothen · D. B. Miracle · C. F. Woodward**

Abstract Compression properties of a refractory multi-component alloy, $Ta_{20}Nb_{20}Hf_{20}Zr_{20}Ti_{20}$, were determined in the temperature range of 296 1473 K and strain rate range of 10^{-1} 10^{-5} s^{-1}. The properties were correlated with the microstructure developed during compression testing. The alloy was produced by vacuum arc melting, and it was hot isostatically pressed (HIPd) and homogenized at 1473 K for 24 h prior to testing. It had a single-phase body-centered cubic structure with the lattice parameter $a = 340.4$ pm. The grain size was in the range of 100 200 μm. During compression at a strain rate of $\dot{\varepsilon} = 10^{-3}$ s^{-1}, the alloy had the yield strength of 929 MPa at 296 K, 790 MPa at 673 K, 675 MPa at 873 K, 535 MPa at 1073 K, 295 MPa at 1273 K and 92 MPa at 1473 K. Continuous strain hardening and good ductility ($\varepsilon \geq 50\%$) were observed in the temperature range from 296 to 873 K. Deformation at $T = 1073$ K and $\dot{\varepsilon} \geq 10^{-3}$ s^{-1} was accompanied by intergranular cracking and cavitation, which was explained by insufficient dislocation and diffusion mobility to accommodate grain boundary sliding activated at this temperature. The intergranular cracking and cavitation disappeared with an increase in the deformation temperature to 1273 and 1473 K or a decrease in the strain rate to $\sim 10^{-5}$ s^{-1}. At these high temperatures and/or low-strain rates the alloy deformed homogeneously and showed steady-state flow at a nearly constant flow stress. Partial dynamic recrystallization, leading to formation of fine equiaxed grains near grain boundaries, was observed in the specimens deformed at 1073 and 1273 K and completed dynamic recrystallization was observed at 1473 K.

Introduction

Metallic alloys with superior mechanical and functional properties at elevated temperatures remain in high demand for the aerospace industry. Operating temperatures of currently used Ni-based superalloys are reaching the theoretical limits, controlled by incipient melting temperatures in the range of 1440 1540 K. New metallic materials with higher melting points, such as refractory molybdenum (Mo) and niobium (Nb) alloys, are examined as alternatives by academic and industrial groups [1 3]. Refractory metals and alloys are a group of metallic materials with melting points above 2123 K. High-temperature strength and creep resistance are the key properties of these alloys, since considerable alloy softening generally occurs at temperatures above ~ 0.5 0.6 T_m, where T_m is the absolute melting temperature. At the same time, poor low-temperature ductility, poor oxidation resistance at elevated temperatures and their high density limit the range of applications of many refractory alloys.

Recently a new strategy for development of high strength and high-temperature alloys, so-called multi-principal-element or high-entropy alloys, has been proposed [4 6]. In these new alloys the configurational entropy of disordered solid solution is maximized by mixing a large number of the alloying elements (generally five or higher) at near-equimolar concentrations. The high entropy of mixing stabilizes more ductile disordered solid solution phases relative to possible intermetallic phases. This concept has shown merit with the production of

O. N. Senkov (✉) · J. M. Scott · S. V. Senkova ·
F. Meisenkothen · D. B. Miracle · C. F. Woodward
Air Force Research Laboratory, Materials and Manufacturing
Directorate, Wright Patterson Air Force Base, OH 45433, USA
e mail: oleg.senkov@wpafb.af.mil

O. N. Senkov · J. M. Scott · S. V. Senkova · F. Meisenkothen
UES, Inc., Dayton, OH 45432, USA

Springer

several experimental alloy compositions with face center cubic (FCC) and/or body center cubic (BCC) crystal structures and favorable combinations of strength and ductility [4 16]. In particular, two refractory high-entropy alloys, $Ta_{25}Nb_{25}Mo_{25}W_{25}$ (TaNbMoW) and $Ta_{20}Nb_{20}V_{20}Mo_{20}W_{20}$ (TaNbVMoW) were recently produced [15, 16], which had a single-phase BCC structure, high hardness of 4.5 and 5.3 GPa, respectively, and very high yield strength ($\sigma_{0.2}$) in the temperature range from 296 to 1873 K. For example, $\sigma_{0.2}$ of 405 and 477 MPa at 1873 K were reported for the TaNbMoW and TaNbVMoW alloys, respectively. Unfortunately, these two refractory alloys have a high density (13.8 g/cm^3 for TaNbMoW and 12.4 g/cm^3 for TaNbVMoW) and are brittle at room temperature. Replacement of heavier W, Mo, and V with lighter Hf, Zr, and Ti allowed formulation of a new refractory alloy, $Ta_{20}Nb_{20}Hf_{20}Zr_{20}Ti_{20}$ (TaNbHfZrTi), with a reduced density of $\rho = 9.94$ g/cm^3 [17]. In the cast and HIP condition, the TaNbHfZrTi alloy had a BCC crystal structure with the lattice parameter $a = 340.4 \pm 0.5$ pm and it showed high-compression yield strength ($\sigma_{0.2} = 929$ MPa), considerable strain hardening and excellent ductility ($\varepsilon > 50\%$) at room temperature [17]. Unfortunately, elevated temperature properties of this alloy were not reported. In this article, the effects of temperature (in the range from 296 to 1473 K) and strain rate (in the range from 10^{-1} s^{-1} to 10^{-5} s^{-1}) on compression properties and microstructure of the TaNbHfZrTi alloy were studied.

Experimental procedures

The TaNbHfZrTi alloy was prepared by vacuum arc melting of the equimolar mixtures of the corresponding elements. Titanium, zirconium, and hafnium were in the form of 3.175 mm diameter slugs with purities of 99.98, 99.95, and 99.9%, respectively. Niobium and tantalum were in the form of 1.0 and 2.0 mm wires, and their purity was 99.95 and 99.9%, respectively. Details of the preparation of this alloy by vacuum arc melting are given elsewhere [17]. The prepared button was about 8 mm thick and had shiny surfaces, indicating no oxidation during vacuum arc melting. The actual alloy composition determined with the use of inductively coupled plasma-optical emission spectroscopy (ICP-OES), is given in Table 1. The cast alloy was hot

isostatically pressed (HIPd) at 1473 K and 207 MPa for 1 h and then vacuum annealed at 1473 K for 24 h.

Cylindrical specimens for compression testing were electric-discharge machined from the HIPd and annealed alloy. The specimen axis was perpendicular to the button surface, which was in contact with the copper plate during arc melting. The specimen surfaces were mechanically polished and the compression faces of the specimens were paralleled and lubricated with boron nitride (for elevated temperature tests). The specimens were ~ 3.8 mm in diameter and ~ 5.7 mm in height. Compression tests were conducted at temperatures 673, 873, 1073, 1273 and 1473 K in a computer-controlled Instron (Instron, Norwood, MA) mechanical testing machine outfitted with a Brew vacuum furnace and silicon carbide dies. Before each test, the furnace chamber was evacuated to 10^{-6} torr. The test specimen was then heated to the test temperature at a heating rate of ~ 20 K/min and soaked at the temperature for 15 min under 5 N controlled load, and then compressed to a 50% height reduction. To study the effect of temperature on the deformation behavior, a constant ramp speed that corresponded to an initial strain rate of 10^{-3} s^{-1} was used. Room temperature testing was conducted at the same loading conditions but in air, and a thin Teflon foil was used between the compression faces and silicon carbide dies to reduce friction. To study the effect of strain rate on the flow stress at 1023 K, constant ramp speeds of 5.7×10^{-1}, 5.7×10^{-2}, 5.7×10^{-3}, 5.7×10^{-4}, and 5.7×10^{-5} mm/s, corresponding to initial strain rate range from 10^{-5} s^{-1} to 10^{-1} s^{-1}, were used. The deformation of all specimens was video-recorded and an optical setup was used to measure strain versus load. The microstructure was analyzed with the use of a scanning electron microscope (SEM) equipped with backscatter electron (BSE), energy dispersive X-ray spectroscopy (EDS), and electron backscatter diffraction (EBSD) detectors.

Results

Compression properties

Effect of temperature

The engineering stress, σ, versus engineering strain, ε curves of the TaNbHfZrTi alloy obtained during compression testing at different temperatures are shown in Fig. 1 and the yield strength values, $\sigma_{0.2}$, at $\varepsilon_p = 0.2\%$, where ε_p is the engineering plastic strain, are given in Table 2. Following yielding, continuous strengthening at nearly constant rate of $\gamma = d\sigma/d\varepsilon = 3360$ MPa (i.e., a 33.6 MPa increase per each 1% of plastic strain) occurred with an increase in the plastic strain at temperatures

Table 1 Chemical composition of the TaNbHfZrTi alloy produced by vacuum arc melting

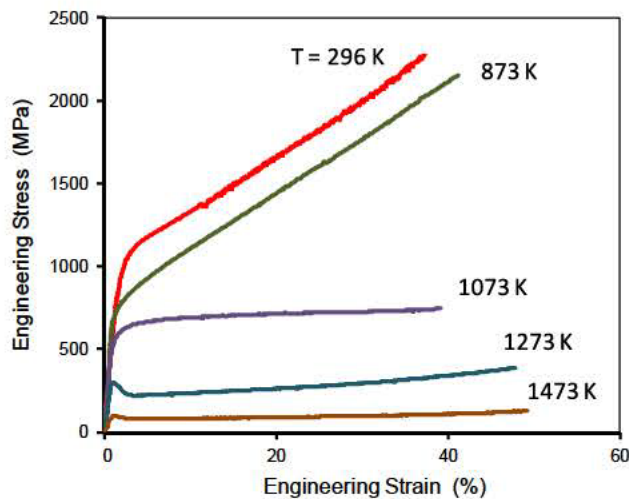| Composition	Ta	Nb	Hf	Zr	Ti
at.%	19.68	18.93	20.46	21.23	19.7
wt. %	30.04	14.84	30.82	16.34	7.96

Fig. 1 Engineering stress vs. engineering strain compression curves of the TaNbHfZrTi alloy at different temperatures
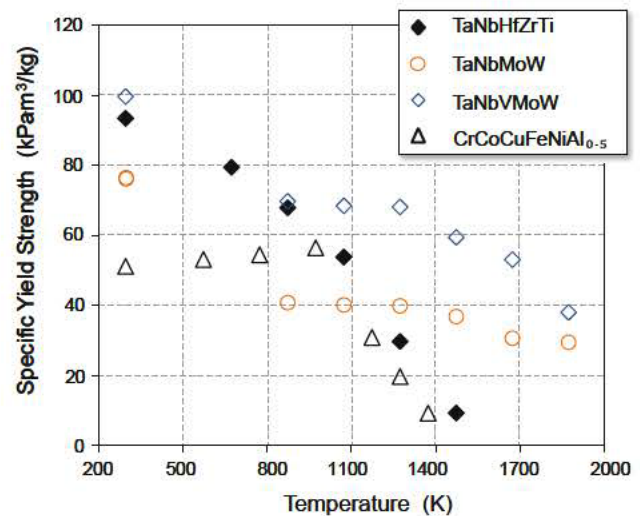

Fig. 2 The temperature dependence of the specific yield strength of the TaNbHfZrTi alloy in comparison with that for TaNbMoW [16], TaNbVMoW [16], and CrCoCuFeNiAl$_{0.5}$ [4] cast alloys

Table 2 Compression yield strength, $\sigma_{0.2}$, of the TaNbHfZrTi alloy at different temperatures

T (K)	296	673	873	1073	1273	1473
$\sigma_{0.2}$ (MPa)	929	790	675	535	295	92

The strain rate is 10^{-3} s^{-1}

296 873 K. At $T = 1073$ K, the strengthening rate decreased to $\gamma \approx 165$ MPa, while at 1273 and 1473 K the alloy showed a drop in the engineering stress after yielding, which was followed by continuous weak strengthening at $\gamma \approx 250$ and 65 MPa, respectively.

The temperature dependence of the specific yield strength (SYS = $\sigma_{0.2}/\rho$) of the studied alloy is shown in Fig. 2. The SYS values of three other recently developed high-entropy cast alloys, high-strength refractory TaNbMoW and TaNbVMoW [16] and a ductile CrCoCuFeNiAl$_{0.5}$ [4], are also given in this figure for comparison. The SYS of the TaNbHfZrTi alloy is about 86% higher at 296 K and about 50% higher at 1273 K than the SYS of the CrCoCuFeNiAl$_{0.5}$ alloy. In the temperature range of 296 1073 K, the SYS of the TaNbHfZrTi alloy is also superior to the SYS of the TaNbMoW alloy. However, the TaNbVMoW is stronger than other three alloys at temperatures from 296 to 1873 K and the TaNbMoW alloy is stronger than TaNbHfZrTi and CrCoCuFeNiAl$_{0.5}$ at temperatures ≥ 1273 K. The rapid drop in the yield strength of the TaNbHfZrTi alloy beyond $T = 1073$ K, compared with the TaNbMoW and TaNbVMoW alloys is apparently due to a much lower melting temperature of the first alloy [16, 17]. A rapid decrease in strength of metallic alloys is known to generally occur at temperatures above

$T_R \sim 0.5$ 0.6 T_m due to intensification of diffusion-related processes [18, 19].

Effect of strain rate

The engineering stress, σ, versus engineering strain, ε curves of the TaNbHfZrTi alloy obtained during compression testing at $T = 1073$ K and different strain rates, $\dot{\varepsilon}$, are shown in Fig. 3. Deformation strengthening occurred and the flow stress increased continuously with an increase in the plastic strain at high-strain rates, $\dot{\varepsilon} = 10^{-1}$ to 10^{-3} s^{-1}. On the other hand, strain softening at the beginning of deformation and steady-state flow at strains
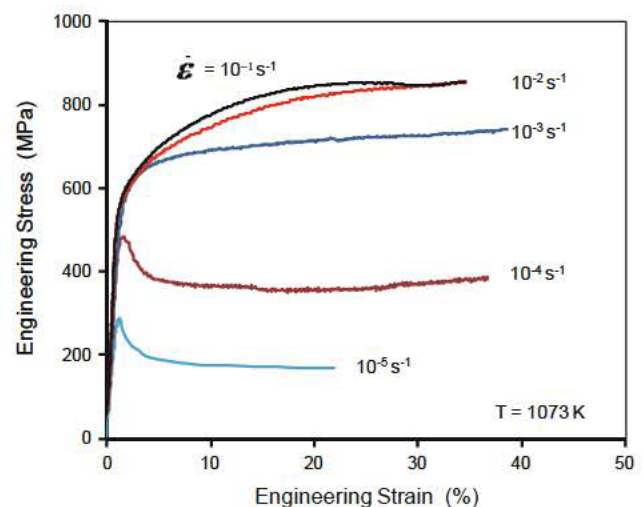

Fig. 3 Engineering stress vs. engineering strain compression curves of the TaNbHfZrTi alloy at T 1073 K and given strain rates
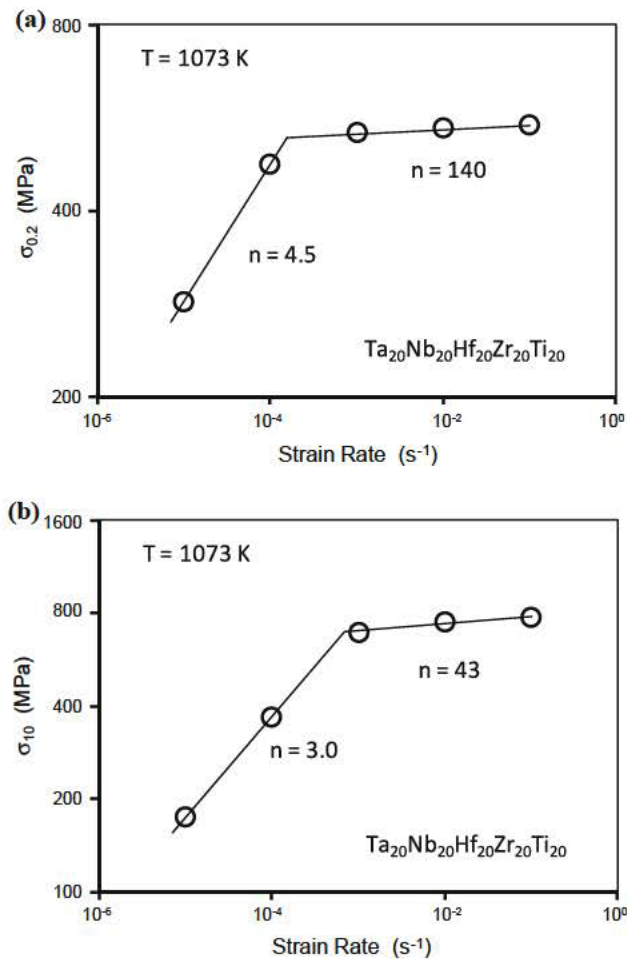
(a)

(b)

Fig. 4 Strain rate dependence of the **a** yield strength, $\sigma_{0.2}$, and **b** flow stress, σ_{10}, at 10% of compression strain of the TaNbHfZrTi alloy at T 1073 K

$$\dot{\varepsilon} = B\sigma^n \qquad (1)$$

where B is a temperature dependent parameter and n is the stress exponent, then for $\sigma_{0.2}$ one can obtain $n = 4.5$ at $\dot{\varepsilon} = 10^{-5}$ 3×10^{-4} s^{-1} and $n = 140$ at $\dot{\varepsilon} = 3 \times 10^{-4}$ 10^{-1} s^{-1}. For σ_{10}, $n = 3.0$ at $\dot{\varepsilon} = 10^{-5}$ 10^{-3} s^{-1} and $n = 43$ at $\dot{\varepsilon} = 10^{-3}$ 10^{-1} s^{-1}.

Microstructure

Microstructure after hot isostatic pressing and annealing

Figure 5 illustrates the microstructure of the TaNbHfZrTi alloy before compression testing (HIPd plus annealed condition). The microstructure consists of equiaxed grains. The grain size is about 100 μm at the bottom side, which was in contact with the chill copper plate, and increases to ~ 200 μm at the top side of the specimen. In spite annealing at 1473 K for 24 h, the element micro-segregation typical to the as-cast condition was still noted inside the grains. In particular, the centers of grains were slightly (~ 2 3%) enriched with Ta and Nb and the regions near grain boundaries were slightly enriched with Hf and Zr, while Ti was almost homogeneously distributed between these regions. The variations in grain sizes did not affect mechanical behavior and the top and bottom parts of the samples showed similar compression behavior (see below).
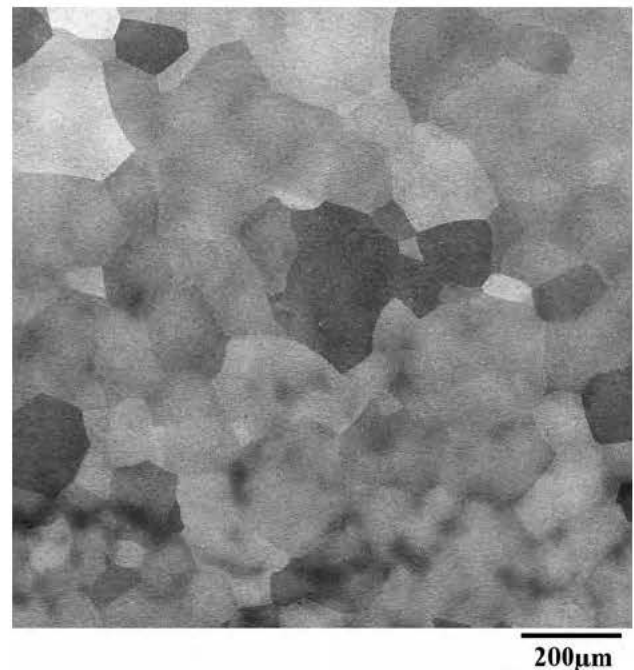
above 5 7% occurred at lower strain rates of 10^{-4} and 10^{-5} s^{-1}. The strain rate dependences of the yield strength, $\sigma_{0.2}$, and the flow stress, σ_{10}, corresponding to $\varepsilon = 10\%$ are shown in Fig. 4a, b, respectively, and the values of $\sigma_{0.2}$ and σ_{10} are given in Table 3. Two distinct regions are clearly seen. Namely, at lower strain rates, both $\sigma_{0.2}$ and σ_{10} increase with an increase in $\dot{\varepsilon}$ more rapidly than at higher strain rates. If a power-law relation between $\dot{\varepsilon}$ and σ is assumed, i.e.,

Table 3 Compression yield strength, $\sigma_{0.2}$, and the flow stress at ε 10%, σ_{10}, of the TaNbHfZrTi alloy at different strain rates, $\dot{\varepsilon}$, and T 1073 K

$\dot{\varepsilon}$ s^{-1} (MPa)	10^{-5}	10^{-4}	10^{-3}	10^{-2}	10^{-1}
$\sigma_{0.2}$	285	475	535	543	550
σ_{10}	175	368	692	746	777

Fig. 5 SEM backscatter electron image of a polished cross section of the arc melted TaNbHfZrTi alloy after HIP and annealing at 1473 K

Microstructure after deformation at $\dot{\varepsilon} = 10^{-3} \, s^{-1}$

Figure 6 shows SEM backscatter images of a longitudinal cross-section of a TaNbHfZrTi alloy specimen compressed by 50% at room temperature. A rather uniform deformation, with a very small specimen barreling and no evidence of strain localization, occurs (Fig. 6a). Deformed grains are elongated in the directions of plastic flow (Fig. 6b). Higher magnification images reveal fine lamellae inside the grains (Fig. 6c). Complimentary electron backscatter diffraction (EBSD) analysis [20] suggests that these lamellae are likely the mixture of distorted deformation twins and shear bands.

Figure 7 illustrates the microstructure of a specimen deformed at 673 K. The deformation is localized in a shear band propagating from the left top side to the right bottom side of the compressed sample (Fig. 7a). Heavy deformation of grains inside the shear band is clearly seen at a higher magnification in Fig. 7b. The shear bands are also developed during deformation at 873 K, however, the strain localization is less pronounced. Instead of one, two crossing shear bands form at this temperature (Fig. 8a) and cracks develop in one of the shear bands after 50% compression strain (Fig. 8b). Deformation twins are observed

in specimens deformed at 673 and 873 K and micro-cracks are occasionally seen at grain boundaries intersecting the twins (Figs. 7c, 8c).

Extensive deformation-induced intergranular cavities and cracks are observed in a specimen deformed at 1073 K (Fig. 9a, b). Higher number density and larger size of these cavities at the side edges of the specimen are likely associated with higher stress concentrations in these regions. No deformation twins are observed at this and higher temperatures. Instead, nanometer-size particles/grains are formed along grain boundaries (Fig. 9c).

Figure 10 shows the microstructures of specimens after 50% compression strain at 1273 and 1473 K. No shear bands, deformation twins or intergranular cracks are observed in these specimens (Fig. 10a). Higher magnification images of the specimen deformed at 1273 K show darker and lighter spots and/or curvy bands inside the deformed grains (Fig. 10b) and a fine-grained structure formed near the grain boundaries (Fig. 10b, c). The new grains are equiaxed and their size is about 1–2 μm at 1273 K. The dark/light spot/band contrasts inside the deformed grains are identified using the EBSD analysis to be likely caused by different electron channeling conditions from these slightly misoriented grain regions [20, 21].
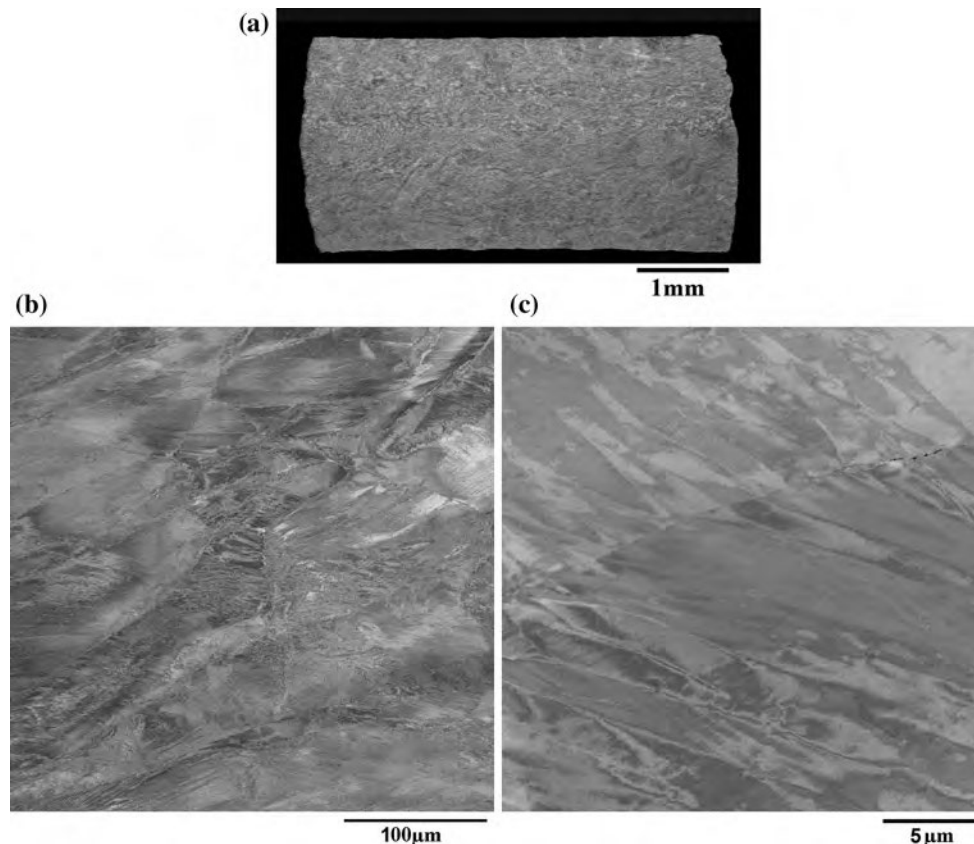

Fig. 6 SEM backscatter images of a longitudinal cross section of the TaNbHfZrTi alloy after 50% compression at 296 K: **a** a low magnification view of the deformed sample, **b** heavily deformed grains, **c** deformation twins/shear bands inside the grains. $\dot{\varepsilon} \approx 10^{-3} s^{-1}$
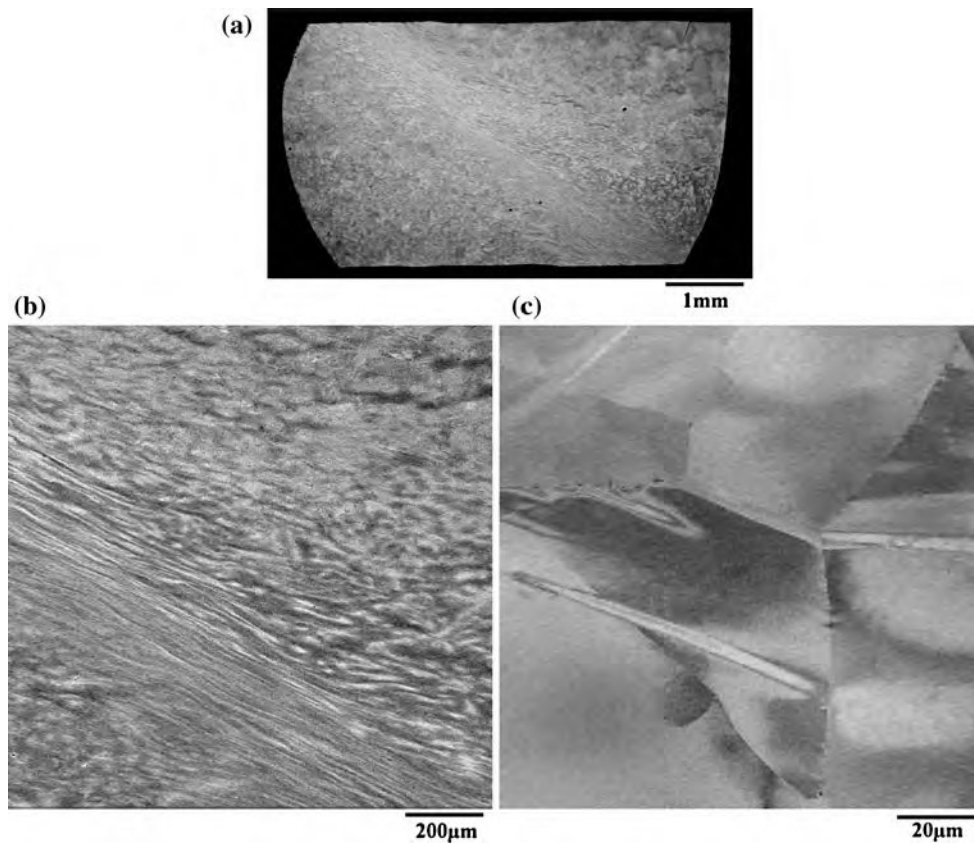
Fig. 7 SEM backscatter images of the longitudinal cross section of the TaNbHfZrTi alloy after 50% compression strain at 673 K. **a** A low magnification view of the deformed sample, **b** microstructure of a heavily deformed region, **c** microstructure of a weakly deformed region (from the top right side of Fig. 7a) showing deformation twins crossing grains. $\dot{\varepsilon}$ 10^{-3} s^{-1}

Fine equiaxed grain structure, with the average grain size of ~ 20 μm, is present in the specimen deformed at 1473 K, which indicates dynamic recrystallization occurring at this temperature.

Effect of strain rate on microstructure after deformation at T = 1073 K

SEM backscatter images of a TaNbHfZrTi alloy specimen after 50% compression strain at 1073 K and $\dot{\varepsilon} = 10^{-2}$ s^{-1} are shown in Fig. 11. The deformed specimen looks somewhat similar to the specimen compressed at the same temperature with $\dot{\varepsilon} = 10^{-3}$ s^{-1} (see Fig. 9). In particular, cracks and cavities are developed at grain boundaries, especially at those oriented about 40 50° to the compression direction (Fig. 11a). Higher magnification images show new fine grains/particles developed in highly deformed regions near the grain boundaries of the deformed grains, as well as elongated sub-grains inside these deformed grains (Fig. 11b, c).

A decrease in the strain rate to $\dot{\varepsilon} = 10^{-4}$ s^{-1} leads to a considerable transformation of the fracture mechanism (Fig. 12). Instead of wedge-shaped cracks typical at higher strain rates (see Figs. 9, 11), mainly spherical cavities are formed at and near grain boundaries in the specimen deformed at $\dot{\varepsilon} = 10^{-4}$ s^{-1} (Fig. 12a, b). Wedge-shaped cracks are also present at triple grain junctions, but these cracks are much smaller and they do not propagate much along grain boundaries. A nearly equiaxed subgrain structure develops inside the deformed grains. New fine grains and lens-shaped cavities at grain boundaries, as well as fine precipitation along subgrain boundaries, are clearly seen in Fig. 12c. The X-ray and SEM/EDS/EBSD techniques used in this study were not capable to identify the chemistry and crystal structure of these second-phase nano-precipitates due to their very small size and low number-density. Transmission electron microscopy is needed for the detailed analysis of these precipitates, which is beyond of the scope of this article.

Discussion

At least three temperature regions with different deformation behavior of the TaNbHfZrTi alloy can be clearly identified. In the temperature range of 296 873 K, the alloy demonstrates strong strain hardening, good ductility
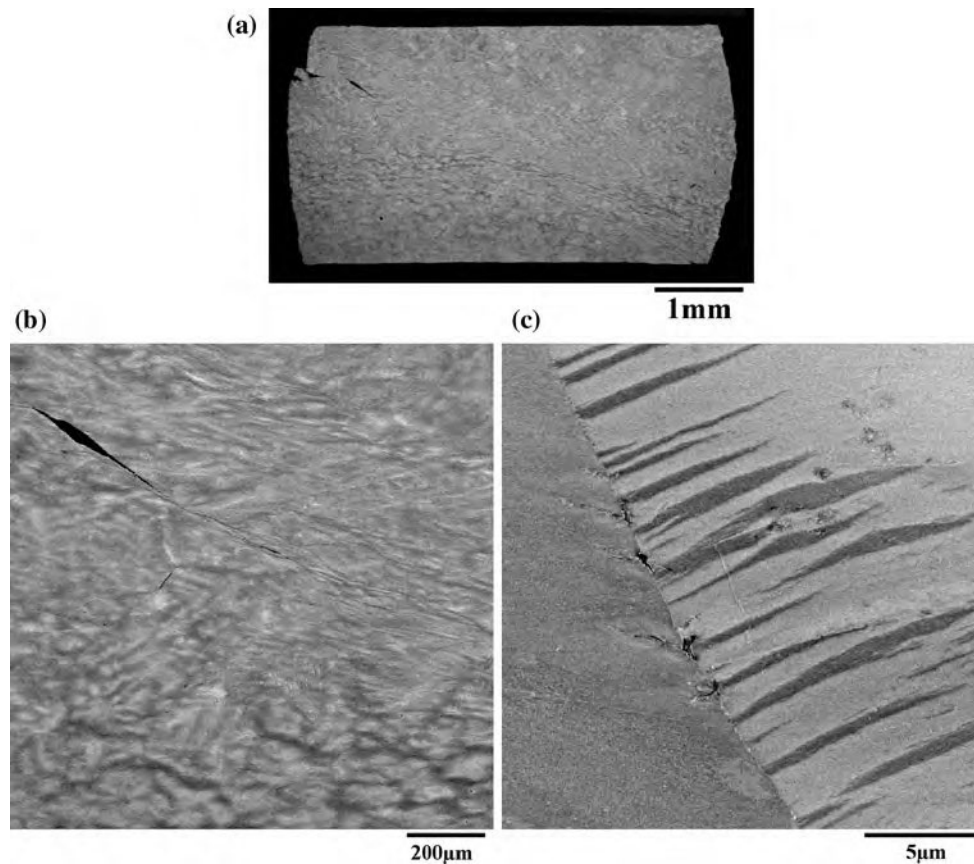
Fig. 8 SEM backscatter images of the longitudinal cross section of the TaNbHfZrTi alloy after 50% compression strain at 873 K. **a** A low magnification view of the deformed sample, **b** microstructure of a shear band with a sharp crack, **c** microstructure of a weakly deformed region (from the top right side of Fig. 8a) showing deformation twins initiated from a grain boundary and ended inside the grain, as well as micro cracks at the grain boundary. $\dot{\varepsilon}$ $10^{-3} s^{-1}$

and deformation twin activity. At 1073 K it exhibits heavy cavitation at grain boundaries, formation of very fine grains along grain boundaries and precipitation of second-phase nano-particles at grain and subgrain boundaries. During deformation at 1273 and 1473 K, the alloy shows a rapid drop in the stress after yielding followed by steady-state flow, formation of new grains near grain boundaries and a subgrain structure inside the original grains at 1273 K, and dynamic recrystallization with the formation of fine, equiaxed grain structure at 1473 K.

Behavior at $T = 296$ 873 K

Typically, five independent slip systems have to be activated to accommodate macroscopic deformation of a polycrystalline alloy. In BCC alloys, to which the studied alloy belongs [17], deformation by twinning generally occurs under conditions at which the slip systems and/or dislocation mobility are restricted [22 25]. Under these conditions, twinning may compensate for the lack of independent slip systems and thus support deformation and delay fracture of polycrystalline aggregates. One may

therefore suggest that the activation of deformation twinning contributes to the good ductility of the TaNbHfZrTi alloy in the temperature range of 296 873 K. The high yield strength and strain hardening observed in this temperature range can be due to solid solution strengthening [17], an increase in the number density of immobile dislocations and an effective decrease in the grain size by formation of twin boundaries and shear bands [26, 27]. Whereas dislocation motion is highly sensitive to temperature and the critical resolved shear stress for dislocation glide decreases rapidly with an increase in temperature, the stress to activate twinning has much weaker temperature dependence, mainly through the temperature dependence of the shear modulus of the alloy. Taking this into account and noting that twinning was not observed during compression at temperatures ≥ 1073 K, one may conclude that the critical twinning stress for this alloy, σ_{ctw} is somewhere above 600 MPa. It is worth noting that no twinning and very low ductility were observed in the BCC TaNbMoW and TaNbVMoW alloys, which had $\sigma_{0.2}$ of 1058 and 1246 MPa, respectively, at room temperature [16]. Such different deformation behavior of these two alloys from the
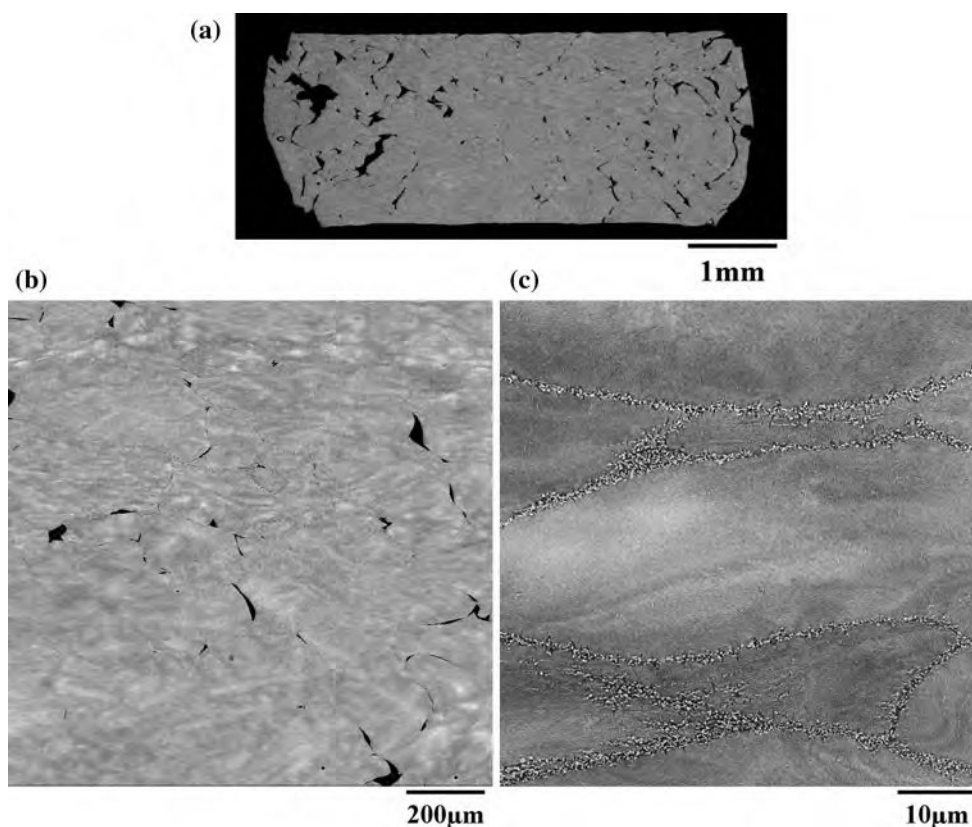
Fig. 9 SEM backscatter images of the longitudinal cross section of the TaNbHfZrTi alloy after 50% compression strain at 1073 K. **a** A low magnification view of the deformed sample, **b** a higher magnification image showing cracks along grain boundaries, **c** fine recrystallized grains along grain boundaries. $\dot{\varepsilon}$ $10^{-3} s^{-1}$

behavior of the TaNbHfZrTi alloy can be explained by their higher stiffness. Indeed, the shear modulus of TaNbMoW and TaNbVMoW alloys is estimated to be ~ 98 and 88 GPa, respectively, while that of the TaNbHfZrTi alloy is ~ 42 GPa [17]. Assuming that σ_{ctw} depends on the composition mainly through the shear modulus and assigning $\sigma_{ctw} = 650$ MPa for the TaNbHfZrTi alloy, one may estimate $\sigma_{ctw} = 1517$ MPa for the TaNbMoW alloy and $\sigma_{ctw} = 1362$ MPa for the TaNbVMoW alloy. These estimates show that σ_{ctw} is much higher than $\sigma_{0.2}$ for both W-containing alloys, thus explaining inactivity of deformation twinning and brittleness in these two alloys.

Behavior at $T = 1073$ K

Extensive cavitation at grain boundaries, as well as grain boundary cracks often emanating from triple grain junctions, observed in the TaNbHfZrTi alloy deformed at 1073 K and high-strain rates ($\dot{\varepsilon} \geq 10^{-3}$ s^{-1}, see Figs. 9 and 11), are likely to be indications of initiation of grain boundary sliding, which is not yet supported by sufficient dislocation mobility and diffusion. It is worth noting that the highest volume fraction of cavities is observed at the side regions of the compressed specimens, which experience the highest tension and shear stresses. Grain boundary sliding results in formation and growth of wedge-shaped cracks at ledges and at triple grain junctions along favorably oriented (about 40 50° to the compression direction) grain boundaries (see Fig. 9a).

The extensive cavitation indicates that the dislocation mobility and diffusion activity are not sufficient to accommodate the grain boundary sliding and relieve stress concentrations at the sliding grain boundaries at these temperature and strain-rate conditions. The distinct tear-and wedge-like morphologies of the cavities in the specimens deformed at $\dot{\varepsilon} = 10^{-2}$ and 10^{-3} s^{-1} suggest that growth of the cavities formed along the inclined grain boundaries occurs by grain separation under the normal tension stresses, and it is unlikely that diffusion-controlled cavity growth occurs. Formation of very fine new grains along the boundaries of deformed grains is an additional indication of the presence of high-internal stresses and high-dislocation density at the grain boundaries. It is quite
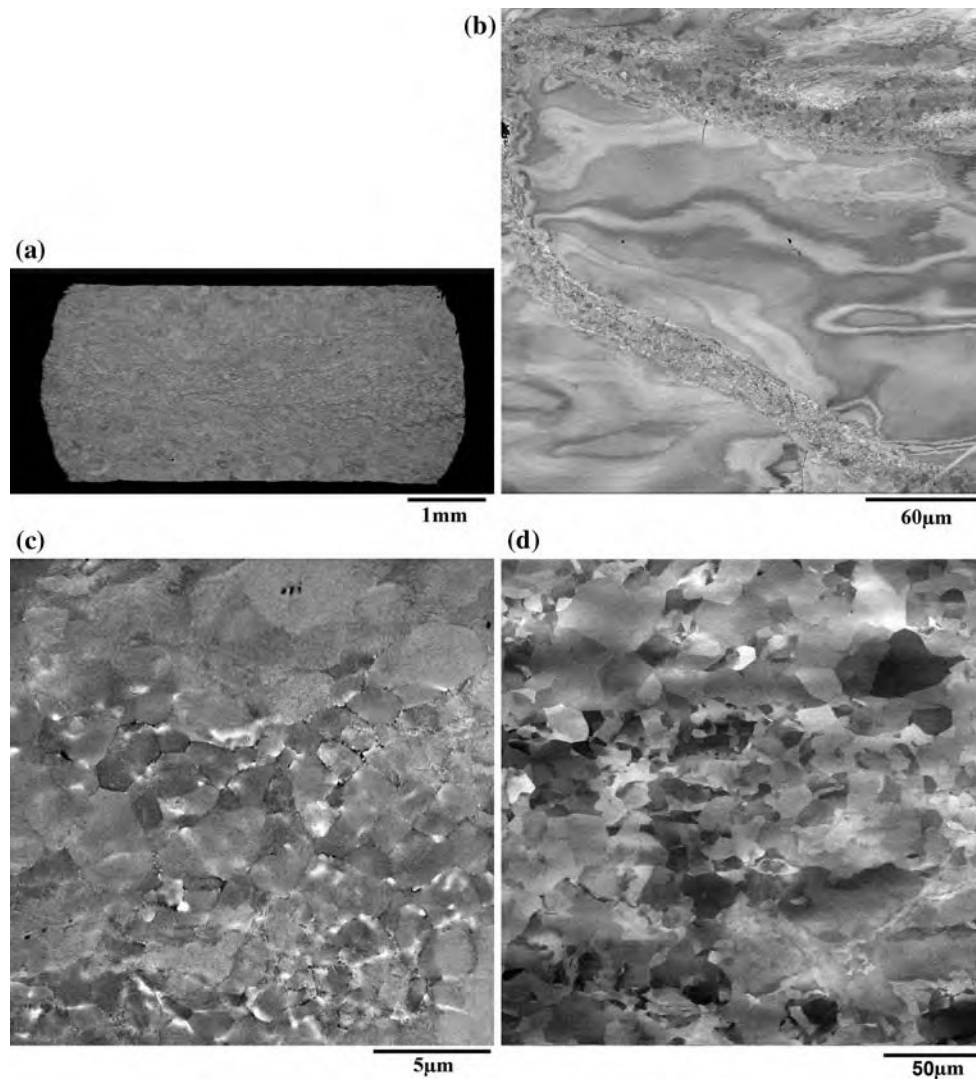
Fig. 10 SEM backscatter images of longitudinal cross sections of the TaNbHfZrTi alloy samples after 50% compression strain at (**a**, **b**, **c**) 1273 K and **d** 1473 K. **a** A low magnification view of the deformed sample, **b** a higher magnification image showing fine recrystallized grains along grain boundaries and electron channeling contrasts inside deformed grains, **c** fine recrystallized grains along grain boundaries and **d** fully recrystallized grain structure. $\dot{\varepsilon}$ $10^{-3} s^{-1}$

possible that as soon as these fresh fine grains are formed, deformation and fracture localize in these fine-grained regions along the initially present grain boundaries. Second-phase nano-particles precipitated near grain boundaries at this temperature may also take part in the grain boundary cavitation, as cracks and voids can be initiated at the particle matrix interfaces during propagation of shear along grain boundaries. Such cavitation behavior is not unique. Some other alloys show similar cavitation and drop in ductility at intermediate temperatures (generally around $\sim 0.5\ T_m$), which are close to the equicohesive temperature, due to initiation of grain boundary sliding not yet accommodated by diffusion processes [28, 29].

A decrease in the strain rate to $\dot{\varepsilon} \leq 10^{-4}\ s^{-1}$ considerably reduces grain boundary cavitation and makes small cavities more round-shaped (see Fig. 12). It is likely that

the rates of diffusion and deformation processes at grain boundaries become comparable at these low-strain rates and the local stress field is not sufficient to control cavitation. Instead, mainly diffusion-controlled cavity growth occurs.

Behavior at $T = 1273\ 1473$ K

Cavitation at grain boundaries disappears when the deformation temperature is increased above 1073 K and no cracks or porosity are observed in the alloy deformed at 1273 and 1473 K (see Fig. 10). Dynamic recrystallization occurs along grain boundaries at 1273 K and in a whole sample at 1473 K. It is expected that the diffusion-controlled processes such as dislocation mobility and dynamic recrystallization are sufficient at these temperatures to
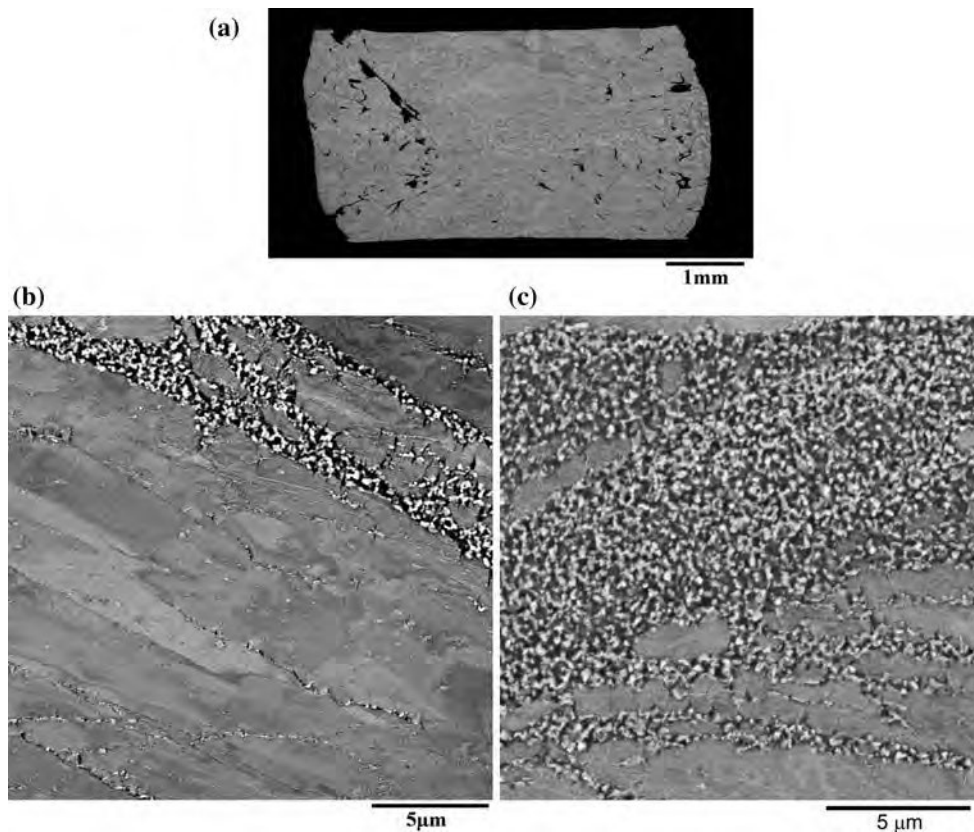
Fig. 11 SEM backscatter images of the longitudinal cross section of the TaNbHfZrTi alloy after 50% compression strain at T 1073 K and $\dot{\varepsilon}$ 10^{-2} s^{-1}. **a** A low magnification view of the deformed sample; **b**, **c** higher magnification images showing **b** fine recrystallized grains/particles along grain boundaries and elongated subgrains inside a deformed grain and **c** fine recrystallized grains/ particles in a heavily deformed region

effectively reduce stress concentrations and prevent formation of cavities at grain boundaries [19, 36]. At the same time, characteristic channeling contrasts observed inside deformed at 1273 K grains spotlight the presence of internal stresses inside these grains. Fortunately, the absence of second-phase particles offers no choice for transgranular fracture at these temperatures.

Effect of strain rate on deformation behavior

The analysis of the deformation behavior and microstructure/fracture features clearly indicates that the mechanisms controlling the deformation and fracture of the alloy at 1073 K dramatically change when the strain rate decreases below 10^{-3} s^{-1}. Indeed, the change in the deformation mechanism with a decrease in $\dot{\varepsilon}$ below 10^{-3} s^{-1} is clearly identified by an abrupt decrease in the stress exponent n (Equation 1) from $n = 140$ to $n = 4.5$ for $\sigma_{0.2}$ and from $n = 43$ to $n = 3.0$ for σ_{10} (see Fig. 4). The very weak dependence of the flow stress on strain rate at high-strain rate values can also be seen in Fig. 4, where the deformation curves obtained at different strain rates are shown. The high n values, indicating a very low strain-rate

sensitivity of the flow stress, typically correspond to thermally activated dislocation glide and originate from the strong exponential dependence of the dislocation velocity on the applied stress [30]. In this regime, that generally occurs at high strain rates and/or low temperatures, a small increase in the flow stress results in a large increase in the dislocation velocity and, respectively, strain rate. The stress exponent value $n = 4.5$ is normally observed during high-temperature dislocation creep, when the dislocation climb is the rate-controlling mechanism [31, 32]. Finally, $n = 3.0$ is generally observed for the solute-drag controlled dislocation glide during high-temperature deformation of solid solutions [33]. Grain boundary sliding accommodated by dislocation climb/glide can also lead to low n values varying from $n = 2$ (when grain boundary sliding is the rate-controlling mechanism) to $n = 4.5$ 5 (when the sliding is controlled by dislocation glide/climb) [34, 35]. Cavitation, observed at 1073 K and described above, starts to develop at strains above 10% and thus should not have effect on $\sigma_{0.2}$ and σ_{10}. Taking into account that a decrease in strain rate affects deformation behavior somewhat similar to an increase in temperature (this is generally described through a temperature-compensated strain-rate
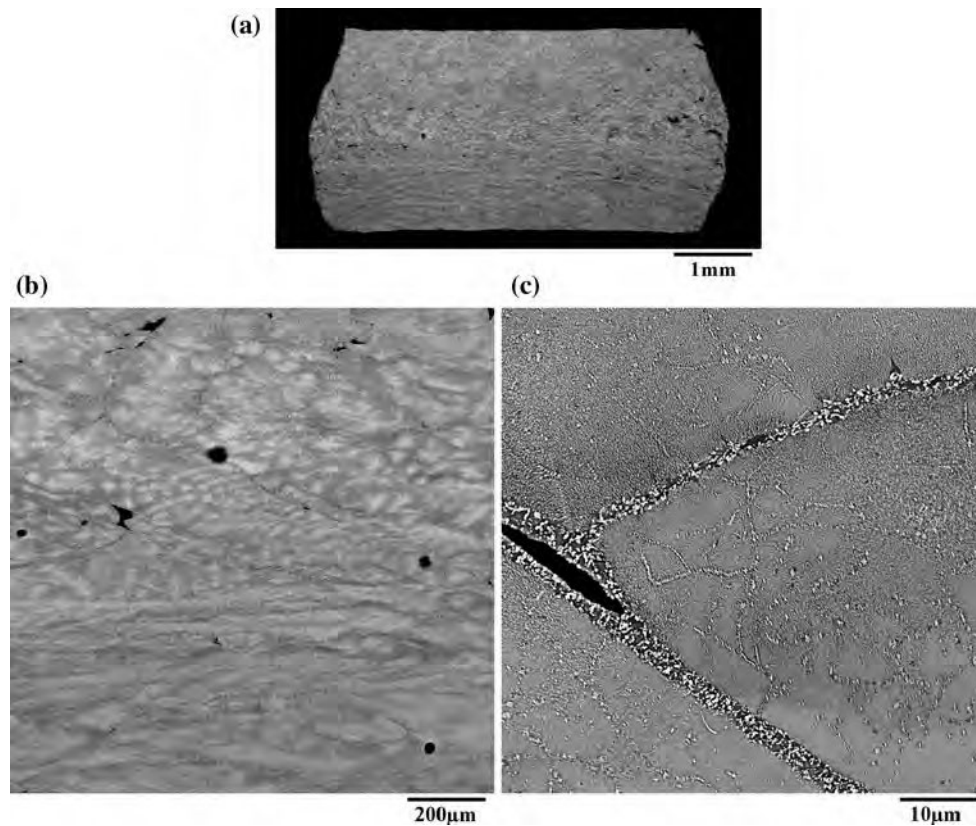
Fig. 12 SEM backscatter images of longitudinal cross sections of the TaNbHfZrTi alloy after 50% compression strain at T 1073 K and $\dot{\varepsilon}$ 10^{-4} s^{-1}

parameter $Z = \dot{\varepsilon}$ $\exp(Q/RT)$, where Q is the activation energy and R is the gas constant [18, 19, 36]), one may suggest from this analysis that at $\dot{\varepsilon} \leq 10^{-3}$ s^{-1} and $T \geq 1073$ K the mechanisms controlling flow stress of the alloy are likely the dislocation climb, solute-drag controlled dislocation glide, and grain boundary sliding. All these mechanisms are diffusion controlled, thus indicating that diffusion becomes sufficient to accommodate deformation at these conditions.

The regression analysis of the experimental data shows that the stress dependence of the Z parameter at $T \geq$ 1073 K and $\dot{\varepsilon} \leq 10^{-3}$ s^{-1} can be described as:

$$Z \equiv \dot{\varepsilon} \exp(Q/RT) = A\sigma^n \qquad (2)$$

where $n = 3.3 \pm 0.3$, $Q = 226 \pm 20$ kJ/mol and $A = (43.0 \pm 3.4) \times 10^{-3}$ MPa^{-n} s^{-1}. An excellent fit ($R^2 = 0.995$) of Eq. 2 to the experimental flow stress values is shown in Fig. 13. The obtained value for the activation energy can be compared with the activation energies for self-diffusion of BCC elements, $Q_{Ta} = 460$ kJ/mol [37]; $Q_{Nb} = 310$ 340 kJ/mol [38]; $Q_{Hf} = 162$ 183 kJ/mol [39]; $Q_{Zr} = 109$ 159 kJ/mol [39], 126 kJ/mol [40], 272 kJ/mol [[41], p. 492], 169 278 kJ/mol [42]; and $Q_{Ti} = 130$ 260 kJ/mol [43, 44]. Although the diffusion of the alloying

elements in the multi-component TaNbHfZrTi alloy can be quite different from the self-diffusion, one can speculate that Hf, Zr, and Ti diffuse much faster than Ta and Nb in this alloy and thus the activation energy of the plastic flow is likely controlled by diffusion of these (Hf, Zr, and/or Ti) elements. Acceleration of the diffusion processes at $T \geq 1073$ K and $\dot{\varepsilon} \leq 10^{-3}$ s^{-1} is also reflected in changing the fracture mechanism from crack propagation at lower temperatures and higher strain rates to void formation and growth at higher temperatures and lower strain rates.

Conclusions

Compression properties of a new refractory multi-component alloy, TaNbHfZrTi, were determined in the temperature range of 296 1473 K and strain rate range of 10^{-1} 10^{-5} s^{-1}. The properties were correlated with the microstructure developed during compression testing. Three temperature regions with different deformation behavior were identified.

In the temperature range of 296 873 K, the alloy showed temperature-independent strain hardening, deformation twinning and shear band formation. High yield
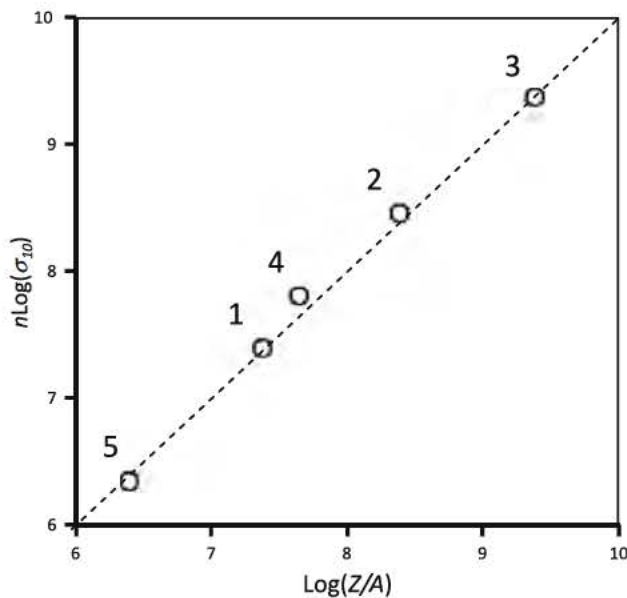
Fig. 13 The relationship between the flow stress σ_{10} and the temperature compensated strain rate parameter $Z \equiv \dot{\varepsilon} \exp(Q/RT)$, in accord to Eq. 4, with n 3.3, Q 226 kJ/mol and A 0.043 MPa^{-n} s^{-1}. The temperatures and strain rates are: *1 T* 1073 K, $\dot{\varepsilon}$ 10^{-5} s^{-1}; *2 T* 1073 K, $\dot{\varepsilon}$ 10^{-4} s^{-1}; *3 T* 1073 K, $\dot{\varepsilon}$ 10^{-3} s^{-1}; *4 T* 1273 K, $\dot{\varepsilon}$ 10^{-3} s^{-1}; *5 T* 1473 K, $\dot{\varepsilon}$ 10^{-3} s^{-1}

strength ($\sigma_{0.2} = 929$ MPa), strong work hardening ($d\sigma/d\varepsilon = 3360$ MPa), homogeneous macroscopic flow and excellent compression ductility ($\varepsilon > 50\%$) were observed at room temperature. Strain localization and formation of deformation shear bands occurred at 673 and 873 K. In this temperature range, macro-cracks were detected only in a specimen deformed at 873 K.

During compression at 1073 K, heavy cavitation and formation of very fine equiaxed grains along the boundaries of deformed grains were observed at strain rates $\geq 10^{-3}$ s^{-1}. No deformation twinning was detected at this temperature. The grain boundary cavitation sufficiently reduced and large notched cracks replaced with finer round-shaped pores at strain rates $<10^{-3}$ s^{-1}. The cavitation was explained by initiation of grain boundary sliding, which created stress concentrations at grain boundary ledges and triple grain junctions due to insufficient dislocation and diffusion mobility at this temperature.

During deformation at 1273 1473 K, the alloy showed a rapid drop in flow stress after yielding followed by the steady-state flow. No cavitations or cracks were observed in specimens compressed at least up to 50% in this temperature range. Partial (at 1273 K) or complete (at 1473 K) dynamic recrystallization occurred during deformation was likely the process responsible for the strain softening and steady-state flow at these temperatures.

References

1. Subramanian PR, Mendiratta MG, Dimiduk DM, Stucke MA (1997) Mater Sci Eng A239 240:1
2. Bewlay BP, Jackson MR, Zhao JC, Subramanian PR (2003) Metall Mater Trans 34A:2043
3. Perepezko JH (2009) Science 326(5956):1068
4. Yeh J W, Chen S K, Lin S J, Gan J Y, Chin T S, Shun T T, Tsau C H, Chang S Y (2004) Adv Eng Mater 6(5):299
5. Yeh J W (2006) Ann Chim: Sci Mater 31:633
6. Yeh J W, Chen Y L, Lin S J, Chen S K (2007) Mater Sci Forum 560:1
7. Zhou YJ, Zhang Y, Wang YL, Chen GL (2007) Mater Sci Eng A 454 455:260
8. Y.J. Zhou, Y. Zhang, Y.L. Wang, G.L. Chen, Appl. Phys. Lett. 90 (2007) 181904/1 3
9. Zhou YJ, Zhang Y, Wang FJ, Wang YL, Chen GL (2008) J Alloys Compd 466:201
10. Wang YP, Li BS, Ren MX, Yang C, Fu HZ (2008) Mater Sci Eng A 491:154
11. Wang FJ, Zhang Y (2008) Mater Sci Eng A 496:214
12. Wen LH, Kou HC, Li JS, Chang H, Xue XY, Zhou L (2009) Intermetallics 17:266
13. Tsai CW, Tsai MH, Yeh JW, Yang CC (2010) J Alloys Compd 490:160
14. Zhu JM, Fu HM, Zhang HF, Wang AM, Li H, Hu ZQ (2010) Mater Sci Eng A527:6975
15. Senkov ON, Wilks GB, Miracle DB, Chuang CP, Liaw PK (2010) Intermetallics 18:1758
16. Senkov ON, Wilks GB, Scott JM, Miracle DB (2011) Intermetallics 19:698
17. Senkov ON, Scott JM, Senkova SV, Miracle DB, Woodward CF (2011) J Alloys Comp 509:6043
18. Dieter GE (1986) Mechanical metallurgy, 3rd edn. McGraw Hill, Inc., New York
19. McQueen HJ, Jonas JJ (1975) In: Treatise on materials science and technology, plastic deformation of materials, vol 6. Academic Press, New York, p 393
20. Senkov ON, Meisenkothen F, Woodward CF (2011) In: Strain localization and deformation twins in a $Ta_{20}Nb_{20}Hf_{20}Zr_{20}Ti_{20}$ high entropy alloy. Air Force Research Laboratory
21. Newbury DE, Joy DC, Echlin P, Fiori CE, Goldstein JI (1986) Advanced scanning electron microscopy and X ray microanalysis. Plenum Press, New York
22. Mughrabi H (1993) In: Materials science and technology, plastic deformation and fracture of materials, vol 6. VCH, Cambridge, p 191
23. Arsenault RJ (1975) Treatise on materials science and technology, plastic deformation of materials, vol 6. Academic Press, New York, p 1
24. Meyers C (1999) Mechanical behavior of materials. Cambridge University Press, Cambridge
25. Christian JW, Mahajan S (1995) Progr Mater Sci 39:1
26. Mulford RA, Kocks UF (1979) Acta Metall 27:1125
27. Meyers MA, Vohringer O, Lubarda VA (2001) Acta Mater 49:4025
28. Cane BJ, Greenwood GW (1975) Metal Sci 9(1):55
29. Riedel H (1987) Fracture at high temperatures. Springer Verlag New York Inc., New York
30. Frost HJ, Ashby MF (1982) Deformation mechanism maps the plasticity and creep of metals and ceramics. Pergamon Press, Oxford

31. Weertman J (1963) Trans AIME 227:1475
32. Weertman J (1968) ASM Trans 61:681
33. Chaudhury PK, Mohamed FA (1987) Metall Trans 18A(1987): 2105
34. Langdon TG (1982) Metall Trans 13A:689
35. Sherby OD, Wadsworth J (1989) Progr Mater Sci 33:169
36. Jonas JJ, Sellars CM, Tegart WJM (1969) Met Rev 14: 1
37. Eager RL, Langmuir DB (1953) Phys Rev 89:911
38. Giithoff F, Hemion B, Herzig C, Petry W, Schober HR, Trampenau J (1994) J Phys: Condens Matter 6:6211
39. Davis BE, McMullen WD (1972) Acta Metall 20:593
40. Kidson G, McGurn J (1961) Canad J Phys 39:1146
41. Neikov OD, Naboychenko S, Gopienko VG, Frishberg IV, Lotsko DV (2009) Handbook of non ferrous metal powders: technology and applications. Elsevier, Amsterdam
42. Herzig C, Köhler U, Divinski SV (1999) J Appl Phys 85:8120
43. Nakamura H, Koiwa M (1991) Iron Steel Inst Jpn Int 31:757
44. Lazarus D (1965) Diffusion in body centered cubic metals. ASM, Cleveland, p 155